SCIENTIFIC REPORTS

OPEN

SUBJECT AREAS:
TWO-DIMENSIONAL MATERIALS
MATERIALS FOR ENERGY AND CATALYSIS

Received
12 December 2013

Accepted
24 January 2014

Published
14 February 2014

Correspondence and requests for materials should be addressed to T.C. (taochen@phy.cuhk.edu.hk)

Few-Layer $MoSe_2$ Possessing High Catalytic Activity towards Iodide/Tri-iodide Redox Shuttles

Lawrence Tien Lin Lee, Jian He, Baohua Wang, Yaping Ma, King Young Wong, Quan Li, Xudong Xiao & Tao Chen

Department of Physics, The Chinese University of Hong Kong, Shatin N. T., Hong Kong, P. R. China.

Due to the two-dimensional confinement of electrons, single- and few-layer $MoSe_2$ nanostructures exhibit unusual optical and electrical properties and have found wide applications in catalytic hydrogen evolution reaction, field effect transistor, electrochemical intercalation, and so on. Here we present a new application in dye-sensitized solar cell as catalyst for the reduction of I_3^- to I^- at the counter electrode. The few-layer $MoSe_2$ is fabricated by surface selenization of Mo-coated soda-lime glass. Our results show that the few-layer $MoSe_2$ displays high catalytic efficiency for the regeneration of I^- species, which in turn yields a photovoltaic energy conversion efficiency of 9.00%, while the identical photoanode coupling with "champion" electrode based on Pt nanoparticles on FTO glass generates efficiency only 8.68%. Thus, a Pt- and FTO-free counter electrode outperforming the best conventional combination is obtained. In this electrode, Mo film is found to significantly decrease the sheet resistance of the counter electrode, contributing to the excellent device performance. Since all of the elements in the electrode are of high abundance ratios, this type of electrode is promising for the fabrication of large area devices at low materials cost.

Chalcogenide derivatives of molybdenum (Mo), e.g. MoS_2 and $MoSe_2$, possess layered structures, where the strong chemical bond forms within each layer (in-plane) while the weak out-of-plane van der Waals force exists across the layers[1,2]. This structural characteristic allows the transformation of the bulk materials into single- or few-layered nanostructures by either top-down exfoliation methods or bottom-up chemical synthesis approaches[1,3–5]. In the reduced dimension, these materials display unprecedented mechanical, optical, electronic and chemical properties[2,6,7]. Such intriguing properties have enabled several classes of applications in catalytic hydrogen evolution reaction[8], field effect transistor[9], near-infrared photothermal agents[10], etc[2,11,12]. In addition to their outstanding properties, the research interests in the molybdenum dichalcogenide also lies in that all the constituent elements are of high abundance ratios in the earth crust, ensuring sustainable resources for the future mass production at low cost.

Herein, we explore a new application of few-layer $MoSe_2$ in catalyzing the reduction of I_3^- to I^- for dye-sensitized solar cells (DSSCs). A typical DSSC consists of a photoanode, which is usually a dye-anchored mesoporous TiO_2 film on fluorine-doped tin oxide (FTO) coated glass, and a counter electrode (CE) with platinum (Pt) nanoparticles on FTO surface as catalyst to facilitate the regeneration of reduced species in the electrolyte[13,14]. In this device structure, the Pt catalyst is featured as a scarce and high-cost element[13]. In addition, the FTO coated glass contributes about 60% of the total cost[15]. Therefore, to develop both Pt- and FTO-free CE is of critical significance in terms of cost-effective practical applications. To date, many efforts have been made to the development of alternative catalyst and FTO-free conducting substrate[16]. Some of the materials based on carbon[17–20], inorganic semiconductors (ceramics)[21–27] and polymer[28] show promising catalytic properties to replace the conventional Pt nanoparticles. However, the attempts on the development of FTO-free conducting substrate have not been successful. Polymer, metal nanostructures and carbon materials are explored for the potential applications as the conducting substrates, but they generally suffer from high resistance[29–31], leading to poorer performance when compared with the traditional FTO. In fact, there has not been a type of both Pt- and FTO-free counter electrode outperforming the conventional Pt nanoparticles on FTO surface for DSSCs. Herein we demonstrate for the first time that few-layer $MoSe_2$ on Mo film as CE shows better performance than the conventional CE based on Pt nanoparticles deposited on FTO.

Results

The fabrication of few-layer $MoSe_2$ on Mo film was conducted by selenizing the Mo-coated soda-lime glass (Mo/glass) in a tube furnace using Ar as carrier gas (Figure 1a). The as-prepared Mo film exhibits body-centered cubic (*bcc*) crystal structures on the ground of X-ray diffraction (XRD) analysis (Figure S1), and the thickness of the Mo film was controlled to be ~1 μm. Optimizations show that the selenization conducted at 550°C for around 5 min generates the best device performance. In principle, the formation of Mo-Se bond could lead to a gradual volume expansion (Figure 1b). Obviously, the limited volume is not able to afford a high-degree expansion; the surface cracking finally drives the formation of $MoSe_2$ nanostructures. The cross-sectional scanning electron microscopy (SEM) image shows that the thickness of the $MoSe_2$ layer is about 70 nm (Figure 1c). The surface of the selenized Mo/glass is composed of many plate-like nanoparticles (Figure 1d). The high resolution transmission electron microscopy (HRTEM) image of the selenized sample presents that there are few-layer structures at the edge of the nanostructures (Figure 1e); the high energy edge site is believed to be catalytically active[32,33]. Furthermore, the interlayer spacing is measured to be 0.63−0.64 nm (Figure 1f), which falls into the typical value of layered $MoSe_2$[2].

Raman spectroscopy was performed to further study the structure of the as-synthesized products. In the selenized sample, the typical peaks situating at ~240 cm^{-1} and ~286 cm^{-1} are observed (Figure 2a), which corresponds to the A^1_g and E^1_{2g} modes of $MoSe_2$[34]. In the bulk $MoSe_2$, however, the A^1_g mode appears at 242 cm^{-1}. The downshift of 2 cm^{-1} indicates the formation of few-layer $MoSe_2$[34]. To make a comparative investigation, we also synthesized MoS_2 by sulfurizing the Mo substrate in sulphur vapor. As a result, the typical peaks locating at ~380 cm^{-1} and ~408 cm^{-1} in the Raman spectrum (Figure 2b) appeared and they can be ascribed to the in-plane E^1_{2g} and out-of-plane A^1_g oscillation modes of MoS_2, respectively[34]. Compared with

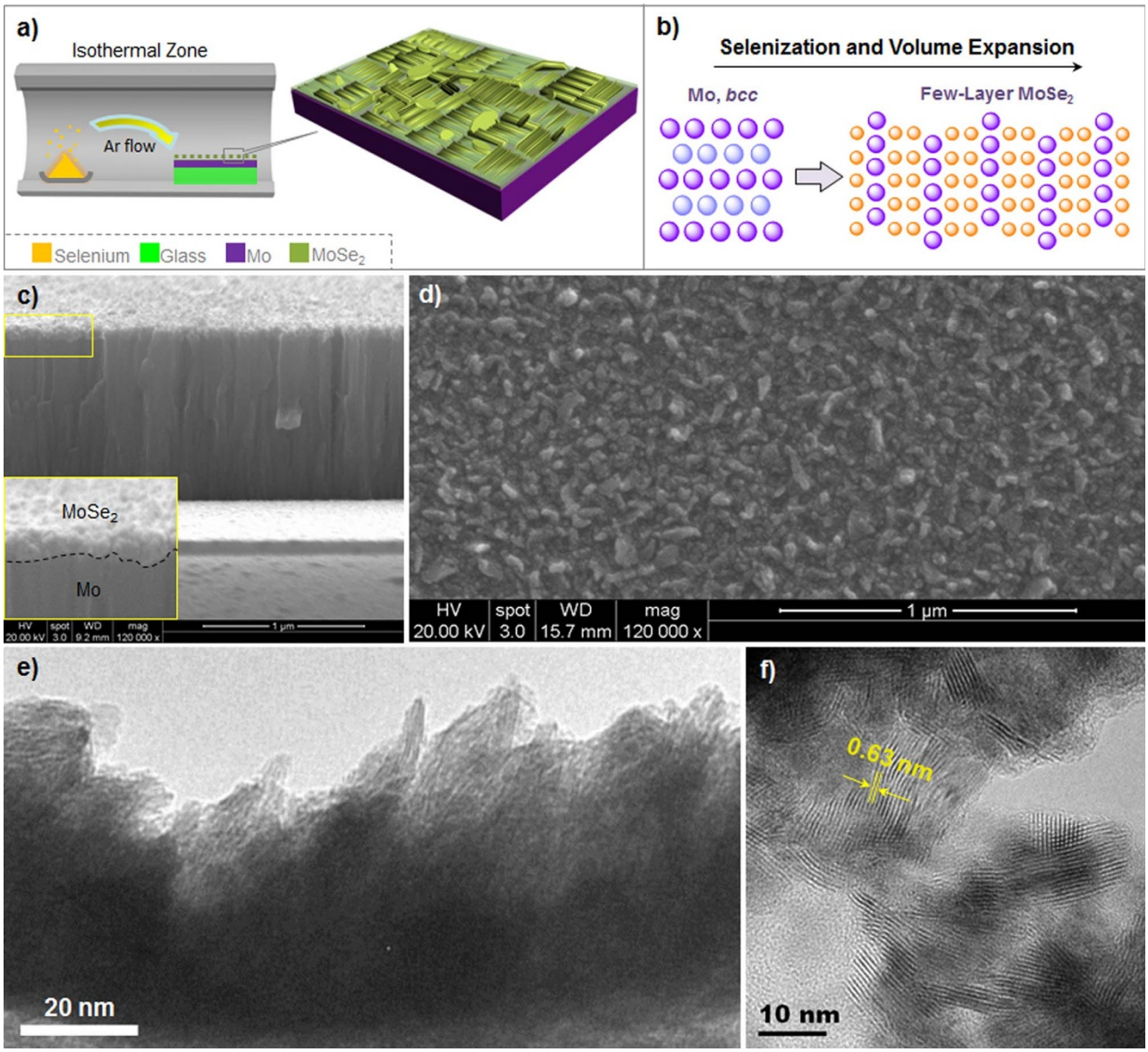

Figure 1 | Scheme of materials synthesis, and structural and morphological characterizations. (a) Schematic setup for the selenization of Mo film on soda-lime glass for few-layer $MoSe_2$ in a furnace tube; (b) Schematic illustration of the formation of few-layer $MoSe_2$ from body-centred cubic Mo, where the volume expansion occurs; (c) Cross-sectional SEM image of the $MoSe_2$ on Mo surface, inset showing an enlarged image with dotted line highlighting the borderline between $MoSe_2$ and Mo substrate; (d) SEM image of the surface morphology of the as-synthesized $MoSe_2$ nanostructures; (e) low magnification HRTEM image of the few-layer $MoSe_2$ on the surface of $MoSe_2$ nanostructures; (f) high magnification HRTEM image of the few-layer $MoSe_2$ with interlayer spacing of 0.63−0.64 nm. HRTEM micrographs in (e) and (f) courtesy of Man Hau Yeung.

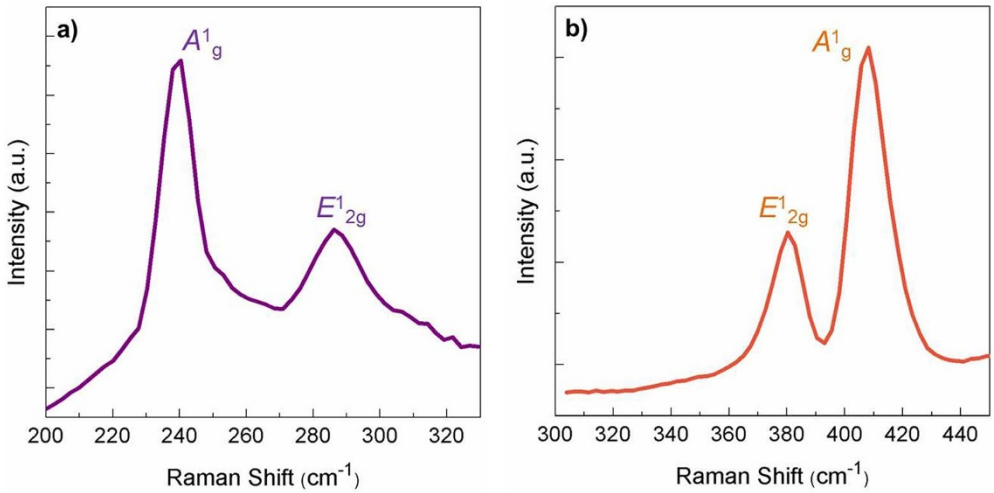

Figure 2 | **Structure characterization.** Raman scattering spectra of the as-synthesized (a) $MoSe_2$ and (b) MoS_2 on Mo substrates.

the bulk MoS_2, the two peaks also show characteristic redshift, indicating the formation of few-layer structures. The positions and intensity ratios of all the Raman peaks of MoS_2 and $MoSe_2$ are consistent with few-layer MoS_2 and $MoSe_2$ in the literature[35,36]. The SEM image of MoS_2 (Figure S2) shows similar morphology to that of $MoSe_2$.

Furthermore, XRD was conducted to study the crystal structures. The XRD patterns of the surface selenized Mo shows only strong signals of Mo, but the signals from $MoSe_2$ are not noticeable, which might be due to the fact that the $MoSe_2$ layer was too thin (~70 nm) to be detected, while the thickness of the Mo layer was about 930 nm (Figure 1c). We thus performed long time annealing at higher temperature for obtaining heavily selenized Mo. As a consequence, the XRD patterns display typical $MoSe_2$ patterns (Figure S1).

Discussion

The major role of CE in DSSC is a catalyst that effectively regenerates the reduced species (e.g. I^-) in electrolyte, but at the same time it also provides a pathway for the photocurrent to complete the circuit. Therefore, both the catalytic properties of the CE towards the redox couple (I^-/I_3^-) and the conductivity of the CE substrate are essential to the CE performance. We firstly conducted cyclic voltammetry (CV) measurement in a three-electrode system to investigate the catalytic property[37,38]. Figure 3a shows the CV profiles using $MoSe_2$/Mo/glass ($MoSe_2$ CE), MoS_2/Mo/glass (MoS_2 CE) and Pt/FTO/glass (Pt CE) as the working electrode, respectively. Two pairs of redox peaks appeared in all the three profiles. The pair of peaks at lower potential (on the left, i.e. Ox 1 and Re 1) is attributed to the oxidation and reduction of iodide/tri-iodide according to equation 1, while the other pair at higher potential (Ox 2 and Re 2) is attributed to redox reaction shown in equation 2[39].

$$I_3^- + 2e^- \rightleftarrows 3I^- \quad (1)$$

$$3I_2 + 2e^- \rightleftarrows 2I_3^- \quad (2)$$

Since the main function of the CE is to catalyse the reduction of tri-iodide (I_3^-) to iodide (I^-), the redox reaction depicted in equation 1 and thus the left pair of peaks is more of our concern. The peak to peak separation (E_{pp}) is in inverse correlation with the standard electrochemical rate constant of the corresponding redox reaction of the two peaks[38]. From Figure 3a, the E_{pp} between Ox 1 and Re 1 for $MoSe_2$ CE, MoS_2 CE and Pt CE can be calculated. As a consequence, the E_{pp} for the $MoSe_2$ CE (313 mV) is lower than that of MoS_2 CE (415 mV), both of which are significantly lower than that in Pt CE (473 mV). This observation implies that the $MoSe_2$ CE has a higher I^-/I_3^- redox rate constant than the MoS_2 CE, and both of them are higher than that of the Pt CE. Such trend can be easily deduced from the peak current density of Re 1 as well. In this regard, the higher reduction peak (i.e. the lower valley) suggests the faster I_3^- reduction rate and thereafter stronger catalytic ability[40]. However, in our case here, the factor of series resistance has to be taken into account when comparing the catalytic properties since different conducting substrates, i.e. Mo and FTO, were applied. This issue will be elucidated later.

Another way to probe the catalytic performance is to employ the symmetrical cell (i.e. sandwich structure CE/electrolyte/CE), which resembles the usual DSSC device structure but without the effect from the dye-loaded TiO_2 anode[41,42], thus it provides a practical environment for testing the CE. In this perspective, Tafel polarization measurements were performed on the symmetrical cells using $MoSe_2$ CE, MoS_2 CE and Pt CE; and the corresponding curves are shown in Figure 3b. Two parameters are obtained from the curve. The intersection of the cathodic branch with the *y*-axis gives the limiting diffusion current density (J_{lim}), which positively correlates with the diffusion coefficient[39]. The J_{lim} values are very similar for all the three cells. The exchange current density (J_0) can be read from the slope of the curves in the Tafel zone, and a larger slope in general indicates a higher J_0 on the CE[43]. Therefore, the Tafel plots suggest that the $MoSe_2$ CE has the highest J_0 and thus seemingly the largest I_3^- reduction rate among the three CEs, followed by MoS_2 CE and Pt CE, which concluded the same trend as from the three-electrode CV profiles.

CV measurements were also performed for the symmetrical cells (with reference electrode short-circuited with counter electrode). The horizontal plateaus in these CV plots (Figure 3c) also show similar J_{lim}. On the other hand, from the inverse slope of the CV curves at zero potential ($V = 0$ V), the overall cell resistance ($R_{sym,\,cell}$) attainable at low current densities could be obtained[41]. The $MoSe_2$ symmetrical cell displays the smallest overall cell resistance while the Pt one exhibits the largest. The lower resistances of the MoX_2 (X = Se, S) cells have benefited from the good conductivity of the Mo substrate (sheet resistance ~ 0.26 Ω sq^{-1}), which is much more conductive than the usual FTO substrate (sheet resistance ~ 12.93 Ω sq^{-1}). In addition, the sheet resistances of $MoSe_2$/Mo and Pt/FTO are measured to be 0.29 and 12.60 Ω sq^{-1} respectively, suggesting that $MoSe_2$/Mo is more favorable as DSSC CE than Pt/FTO from the resistance perspective.

Furthermore, electrochemical impedance spectroscopy (EIS) for symmetrical cells was carried out to examine the details inside the overall cell resistance. The Nyquist plots shown in Figure 3d were fitted by the equivalent circuit as shown in the inset, where R_S is the

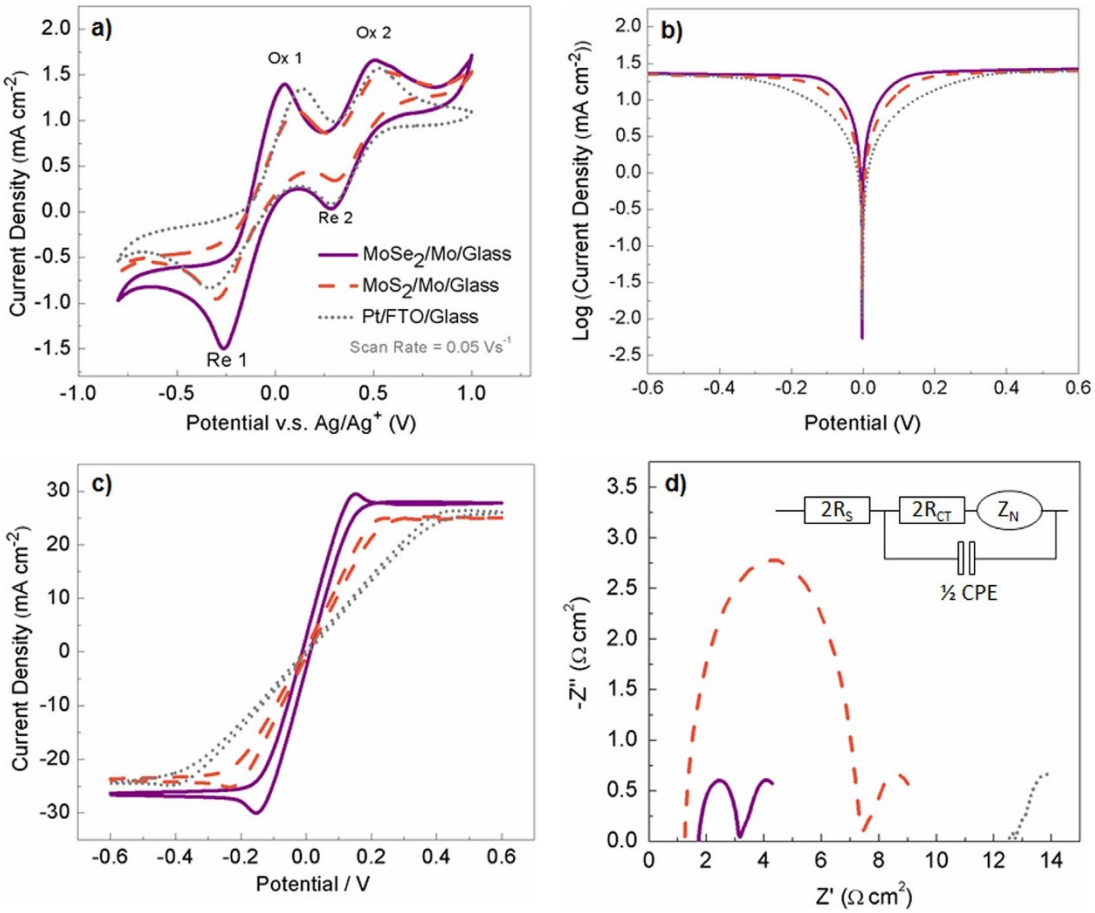

Figure 3 | Electrochemical characterizations. (a) Three-electrode CV using $MoSe_2$ and MoS_2 on Mo/glass and Pt on FTO/glass as working electrode in electrolyte. (b) Tafel plot of symmetrical cell made of $MoSe_2$ and MoS_2 on Mo/glass and Pt on FTO/glass; (c) CV scans of symmetrical cells made of $MoSe_2$ and MoS_2 on Mo/glass and Pt on FTO/glass; (d) EIS of symmetrical cell made of $MoSe_2$ and MoS_2 on Mo/glass and Pt on FTO/glass, inset showing the equivalent circuit for fitting the EIS of the symmetrical cells.

ohmic series resistance ($2R_S$ corresponds to the high frequency intercept of the Nyquist plot), R_{CT} is the charge transfer resistance, CPE is a constant phase element where the electrode surface roughness has been considered in the capacitance ($2R_{CT}$ and 1/2 CPE correspond to the semicircle in the high frequency range, i.e. on the left of the Nyquist plot), and Z_N is the Nernst diffusion impedance (Z_N corresponds to the semicircle in low frequency range, i.e. on the right of the Nyquist plot) in the bulk electrolyte[22,41,42]. Important parameters for the three symmetrical cells are summarized in Table 1. First of all, the Z_N for all three cells are very similar, which is consistent with the J_{lim} results from Tafel plots and CV of the symmetrical cells, since the Nernst diffusion impedance correlates negatively with the diffusion coefficient[39]. On the other hand, the R_S of the $MoSe_2$ cell (0.87 $\Omega \cdot cm^2$) and MoS_2 cell (0.61 $\Omega \cdot cm^2$) are very much lower than that of Pt cell (6.26 $\Omega \cdot cm^2$). Once again this shows the advantage of using Mo as the substrate when compared with FTO. The small R_S is due to the good conductivity of Mo. This also suggests that the contact resistance between the $MoSe_2$ or MoS_2 and Mo should be small as well. Notably, the R_{CT} value of Pt based cell is smaller than both $MoSe_2$ as well as MoS_2 cells, which indicates that the catalytic ability of $MoSe_2$ and MoS_2 towards I_3^- reduction might not be as strong as Pt. However, the high conductivity from the Mo substrate, thus lower series resistance from the $MoSe_2$ and MoS_2 CE, produces favorable effect in the electrochemical catalytic performance. Therefore, the $MoSe_2$/Mo and MoS_2/Mo combinations are finally able to compete with the Pt/FTO as the CE for the DSSCs.

At last, the surface chalcogenized Mo CE were used for DSSC devices. The photocurrent density-voltage (*J-V*) curves are shown in Figure 4 and the photovoltaic performance parameters are tabulated in Table 1. The devices using $MoSe_2$ and MoS_2 CEs produce PCEs of 9.00% and 8.69%, respectively, which are higher than the device using Pt CE (8.68%). Since the photoanodes of all the devices are identical, the difference in device performance should be resulted from the different CEs. Detailed examination shows that the higher fill factor (*FF*) is the main reason for the efficiency improvement (Table 1); while the short-circuit current density (J_{SC}) and open-circuit voltage (V_{OC}) present rather small alternations. *FF* is associated with total resistance of the devices[44,45]. Therefore, the good conductivity of Mo can lead to higher *FF*. The trend of the *FF* among the three devices also matches the overall cell resistance of the symmetrical cells using the corresponding CEs, as well as the DSSC devices' series resistances obtained from the intercepts with the real axis in the Nyquist plot (Figure S4). The V_{OC} of MoS_2 CE device was ca. 0.02 V lower than the Pt CE devices, while the V_{OC} of $MoSe_2$ CE device was similar to the Pt CE counterpart, indicating the efficiency of $MoSe_2$ as catalyst in the CE. The V_{OC} trend is also well confirmed by the EIS results of these DSSCs measured in dark. The devices with larger V_{OC} have larger back charge transfer impedances, i.e. larger low frequency semicircles in the Nyquist plots (Figure S4).

To investigate the structure dependent catalytic property, we performed higher temperature selenization to synthesize the CE; the higher temperature can drive the high-energy edge site and grains rotating and/or migrating and thus the basal face favorably exposing[35].

Table 1 | Photovoltaic and electrochemical performance of the counter electrode. The PCE, V_{OC}, J_{SC} and *FF* of the dye-sensitized solar cells using identical photoanodes with $MoSe_2$ and MoS_2 on Mo-coated soda-lime glass and Pt on FTO glass as counter electrodes; the R_S, R_{CT} and Z_N values of the symmetric cells fabricated using the corresponding electrodes

CE	PCE (%)	V_{OC} (mV)	J_{SC} (mA cm^{-2})	FF (%)	$2R_S$ (Ω cm^2)	$2R_{CT}$ (Ω cm^2)	Z_N (Ω cm^2)
$MoSe_2$/Mo	9.00	746	16.71	72.2	1.74	1.39	2.08
MoS_2/Mo	8.69	726	16.95	70.6	1.21	5.25	2.10
Pt/FTO	8.68	740	17.19	68.3	12.52	0.22	2.26

When the $MoSe_2$ CEs were selenized at 580°C for 60 min and 120 min, the corresponding DSSC device efficiencies are decreased to 7.14% (J_{SC} = 16.14 mA cm^{-2}, V_{OC} = 0.693 V and *FF* = 63.8%) and 4.26% (J_{SC} = 14.72 mA cm^{-2}, V_{OC} = 0.738 V and *FF* = 39.2%) (Figure 4). Apparently, the significantly reduced *FF* and J_{SC} are the reasons for the decreased PCE. In the higher temperature selenized Mo/glass, the thicknesses of $MoSe_2$ are found increased to 360 nm and 400 nm. The increased $MoSe_2$ thickness can generate higher charge transport resistance across the $MoSe_2$ network, thus leading to reduced *FF*. Further inspection show that on the higher temperature selenized samples, the plate-like structures disappeared while the $MoSe_2$ nanoparticle network became dominant (Figure S5), indicating reduced number of edge sites[35]. In the catalytic reaction, the edge site of the 2D material is highly active, while the basal site is not[32,46]. This transformation thus leads to less efficient reduction of I_3^- to I^- for dye regeneration, giving rise to reduced J_{SC} from 16.14 to 14.72 mA cm^{-2} (Figure 4). This is confirmed by selenizing the $MoSe_2$/Mo CE at lower temperature (550°C) but for longer time (180 min). At this temperature there is not sufficient kinetic energy to drive the rotation of edge to basal site[35], thus the corresponding device shows comparable J_{SC} (Figure 4). Instead, the prolonged annealing can most likely facilitate the crystallization of few-layer $MoSe_2$ which improves the catalytic activity for higher J_{SC} (17.57 mA cm^{-2}). All of the above observations confirm that the edge sites are crucial for the high catalytic activity, so engineering the structure with more exposed edge site could further improve the device efficiency.

The scalability of Mo-coated soda-lime glass preparation has been well-established in the CIGS solar technologies. This lays the ground for the large-area fabrication of few-layer $MoSe_2$ CE via the direct selenization. Herein, we performed initial attempt to fabricate a rectangular electrode with surface parameter of 100 mm × 10 mm (Figure 5). The selenization in isothermal tube furnace ensures the identical morphology throughout the Mo substrate (Figure 5b–d and S6), and the uniformity and crack-free surface was shown in the low magnification SEM images (Figure S7). The CE's stability in the I^-/I^{3-} system is preliminarily examined by consecutive CV scanning for 20 cycles. It turns out that the CV curves do not show obvious changes, indicating that the $MoSe_2$ CE could resist the electrolyte corrosion and the applied potential (Figure S8). Furthermore, the devices fabricated with the electrodes from different areas exhibit resemble performance, manifesting the scalability.

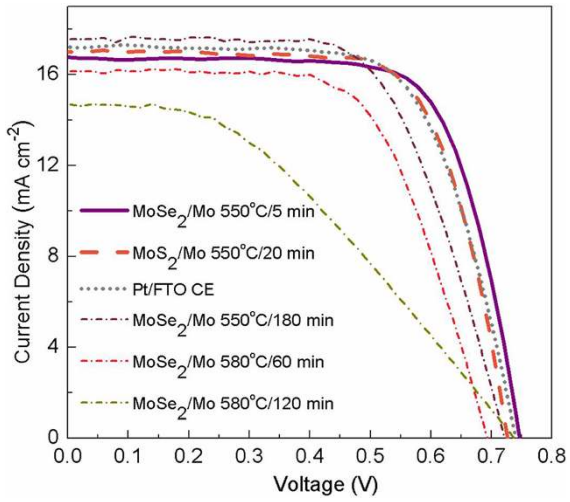

Figure 4 | Photovoltaic property of the devices based on different counter electrodes. Photocurrent-voltage characteristics of the dye-sensitized solar cells using $MoSe_2$ and MoS_2 on Mo/glass with different selenization and sulfurization temperatures and durations and Pt on FTO/glass as counter electrodes.

In summary, for the first time we demonstrate that the use of $MoSe_2$ as catalyst on Mo-based conducting substrate for counter electrode in dye-sensitized solar cell can outperform the conventional Pt on FTO based device. Our method is simple, straightforward and scalable. Notably, all of the elements in the as-developed counter electrode are of high abundance ratios, ensuring sustainable development at low material cost. Compared with the FTO conducting glass, the small sheet resistance of the Mo substrate is particularly attractive for large-area device fabrication. To date, the fabrication of the photoanode can be readily scaled up by screen printing technique, while there has been no method for the large-area fabrication of Pt- and FTO-free counter electrodes. Therefore, this research will pave the way for large scale fabrication of high-efficiency dye-sensitized solar cells at reduced cost.

Methods

Materials. The chalcogenide sources used for sulfurization and selenization were purchased from ACROS (Sulfur, 99.999% trace metal basis, CAS: 7704-34-9) and Aldrich (Selenium pellets, ≥99.99% trace metals basis, CAS: 7782-49-2) respectively, and were used without further purification. Dye *cis*-bis(isothiocyanato)bis(2,2′-bipyridyl-4,4′-dicarboxylato)-ruthenium(II)-bis-tetrabutyl-ammonium (commonly known as N719) powder was purchased from Solaronix. TiO_2 paste with average diameters of 20 nm and 200 nm and iodide-based liquid electrolyte (DHS-E23) were obtained from HeptaChroma.

Preparation of counter electrodes. Mo films were DC-sputtered on a 10 cm × 10 cm soda-lime glass in two steps. In the first step, the sputter power was 75 W and the vacuum pressure was 1 Pa with Ar flow. In the second step, the sputter power increased to 100 W and pressure decreased to 0.15 Pa with Ar flow. About 500 nm molybdenum was deposited in each step. After cutting the Mo sputtered glasses (Mo/glass) into pieces of appropriate sizes, these pieces were ultrasonically cleaned in ethanol and DI water, and then dried by blowing compressed air.

In the chalcogenization, Mo/glass pieces were placed, together with the sulfur pieces/selenium pellets as the chalcogen sources, in a quartz tube furnace pumped down to a base pressure of 10^{-2} mbar. For sulfurization, the furnace was heated to 550°C in 20 min, and held at 550 °C for 20 min, followed by natural cooling with Ar purge and pumping to a pressure of 5×10^{-1} mbar in order to remove the residual sulfur vapor. The selenization process was similar to sulfurization, but only with a shorter (5 min) 550°C holding time and pumping with Ar purge to 2×10^{-1} mbar for the whole process. These chalcogenized Mo/glass (MoS_2/Mo/glass and $MoSe_2$/Mo/glass) pieces were stored in dry box at ~RH 50% before making them into devices.

The reference Pt counter electrode was obtained by sputter coating Pt on FTO at ~13 mA for 180 s with power 150 W.

Fabrication of DSSCs and symmetrical cells. TiO_2 mesoporous films on the photoanodes were prepared according to our reported method[47–49]. These films were deposited on FTO/glass, and consisted of transparent layers (total thickness ca. 12 μm, made up of TiO_2 particles with average diameter of 20 nm) and scattering layer (ca. 6 μm thick, TiO_2 particles with average diameter of 200 nm), with a macroscopic area of 0.196 cm^2. Practically, each layer was printed with the corresponding TiO_2 paste, followed by relaxation (3 min) and short heating (150°C for 6 min) for solidification of that layer. Then the final films were heated gradually to 480°C under hot air flow, and held at 480°C for 45 minutes for burning out the

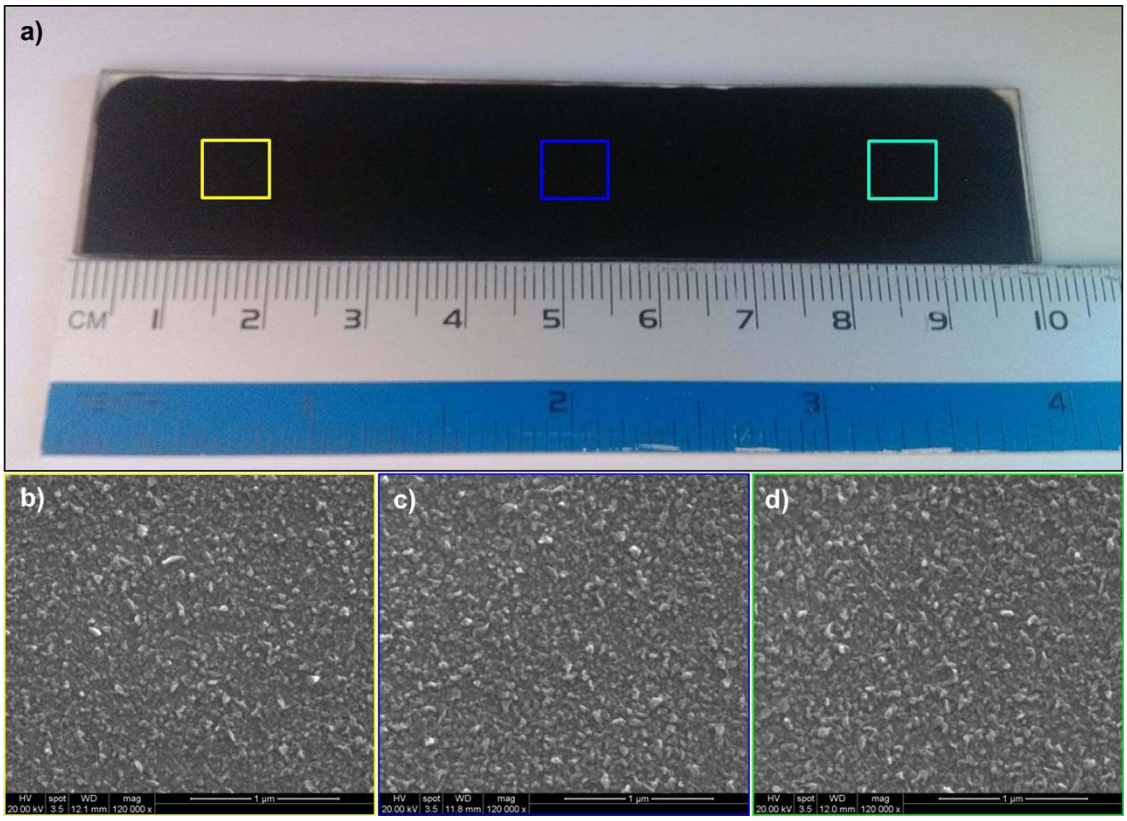

Figure 5 | Scalable fabrication of the $MoSe_2$–based counter electrode. (a) Digital photo of the as-prepared counter electrode with area of 100 mm × 10 mm; (b−d) SEM images of the large-area counter electrodes from different sites. Photograph in part (a) courtesy of Bokai Zhang.

polymer, so that 3D mesoporous network of TiO_2 nanoparticles remained. After that, these sintered films were soaked into 0.02 M TiF_4 aqueous solution at 70°C for 45 min, rinsed in DI water, and further annealed at 450°C for 30 min. Finally, these films were soaked in N719 solution bath (0.5 mM in acetonitrile/t-butanol, 1 : 1 v%) in dark for 17 hours, then rinsed in ethanol and acetonitrile to wash away non-adsorbed dye, dried in air, and the photo-anodes were completed.

To fabricate DSSC device, the photo-anode and counter electrode were assembled into a sandwich type structure, which was sealed by melting parafilm at about 100°C by pressing soldering iron on the structure. Iodide based electrolyte was then injected into the devices, and at last the injecting holes were sealed by tape. The effective areas of all photo-anodes were 0.126 cm^2, defined by the aperture area of the tape masks attached in front of the photo-anode.

For symmetrical cells (or dummy cells), the fabrication procedures were the same as assembling DSSC devices, but only the photo-anodes were replaced by the corresponding CEs in order to make them symmetric.

Characterizations. The cross-sections and surfaces morphology of the counter electrodes were characterized by scanning electron microscopy (SEM; FEI Quanta 400 FEG microscope). The Raman spectra were obtained using RM-1000 Micro Raman Spectrometer (Renishaw) and laser with wavelength 514 nm. The X-ray diffraction (XRD) spectra were scanned by SmartLab X-ray Diffraction System (Rigaku).

To observe the redox reaction peaks in CV spectrums, CV measurement was carried out using 3-electrode method, in which Pt foil was utilized as the counter electrode, Ag/Ag^+ non-aqueous electrode as the reference electrode, and the as-prepared CEs as the working electrodes, in a electrolyte bath with 10 mM LiI, 1 mM I_2, and 0.1 M $LiClO_4$ in acetonitrile. These spectra were measured by Electrochemical Workstation CHI 6009D (CH Instrument) at scan rates of 50 mVs^{-1}. The current density-voltage (*J-V*) characteristics of the assembled DSSCs were measured by a semiconductor characterization system (Keithley 236) at room temperature in air, under the spectral output from solar simulator (Newport) using an AM 1.5G filter with a light power of 100 mW/cm^2. Electrochemical Workstation CHI 760E (CH Instrument) was used to characterize the electrochemical properties of the symmetrical dummy cells, including electrochemical impedance spectroscopy (EIS), Tafel polarization, and cyclic voltammetry (CV). EIS was recorded under dark condition at open circuit over a frequency range of 0.1 to 10^5 Hz with AC amplitude of 10 mV and the fitted parameters were calculated from Z-View software (v2.1b, Scribner AssociatNe, Inc.).

1. Nicolosi, V., Chhowalla, M., Kanatzidis, M. G., Strano, M. S. & Coleman, J. N. Liquid Exfoliation of Layered Materials. *Science* **340**, 1226419-1−1226419-18 (2013).
2. Wang, Q. H., Kalantar-Zadeh, K., Kis, A., Coleman, J. N. & Strano, M. S. Electronics and optoelectronics of two-dimensional transition metal dichalcogenides. *Nat. Nanotechnol.* **7**, 699–712 (2012).
3. Chhowalla, M. *et al.* The chemistry of two-dimensional layered transition metal dichalcogenide nanosheets. *Nat. Chem.* **5**, 263–275 (2013).
4. Zeng, Z. *et al.* Single-Layer Semiconducting Nanosheets: High-Yield Preparation and Device Fabrication. *Angew. Chem. -In. Ed.* **50**, 11093–11097 (2011).
5. Halim, U. *et al.* A rational design of cosolvent exfoliation of layered materials by directly probing liquid–solid interaction. *Nat. Commun.* **4**, 2213 (2013).
6. Jiang, J. W., Zhuang, X. Y. & Rabczuk, T. Orientation Dependent Thermal Conductance in Single-Layer MoS_2. *Sci. Rep.* **3**, 2209 (2013).
7. Terrones, H., Lopez-Urias, F. & Terrones, M. Novel hetero-layered materials with tunable direct band gaps by sandwiching different metal disulfides and diselenides. *Sci. Rep.* **3**, 1549 (2013).
8. Lukowski, M. A. *et al.* Enhanced Hydrogen Evolution Catalysis from Chemically Exfoliated Metallic MoS_2 Nanosheets. *J. Am. Chem. Soc.* **135**, 10274–10277 (2013).
9. Radisavljevic, B., Radenovic, A., Brivio, J., Giacometti, V. & Kis, A. Single-layer MoS_2 transistors. *Nat. Nanotechnol.* **6**, 147–150 (2011).
10. Chou, S. S. *et al.* Chemically Exfoliated MoS_2 as Near-Infrared Photothermal Agents. *Angew. Chem. -In. Ed.* **52**, 4160–4164 (2013).
11. Zhu, C. *et al.* Single-Layer MoS_2-Based Nanoprobes for Homogeneous Detection of Biomolecules. *J. Am. Chem. Soc.* **135**, 5998–6001 (2013).
12. Huang, X., Zeng, Z. & Zhang, H. Metal dichalcogenide nanosheets: preparation, properties and applications. *Chem. Soc. Rev.* **42**, 1934–1946 (2013).
13. Hagfeldt, A., Boschloo, G., Sun, L., Kloo, L. & Pettersson, H. Dye-Sensitized Solar Cells. *Chem. Rev.* **110**, 6595–6663 (2010).
14. Oregan, B. & Gratzel, M. A Low-cost, High-efficiency Solar-Cell Based on Dye-Sensitized Colloidal TiO_2 Films. *Nature* **353**, 737–740 (1991).
15. Lee, K. S. *et al.* Dye-sensitized solar cells with Pt- and TCO-free counter electrodes. *Chem. Commun.* **46**, 4505–4507 (2010).
16. Wu, J. *et al.* A Large-Area Light-Weight Dye-Sensitized Solar Cell based on All Titanium Substrates with an Efficiency of 6.69% Outdoors. *Adv. Mater.* **24**, 1884–1888 (2012).
17. Murakami, T. N. *et al.* Highly Efficient Dye-Sensitized Solar Cells Based on Carbon Black Counter Electrodes. *J. Electrochem. Soc.* **153**, A2255–A2261 (2006).
18. Xiao, Y. *et al.* Pulse electropolymerization of high performance PEDOT/MWCNT counter electrodes for Pt-free dye-sensitized solar cells. *J. Mater. Chem.* **22**, 19919–19925 (2012).
19. Wang, H., Sun, K., Tao, F., Stacchiola, D. J. & Hu, Y. H. 3D Honeycomb-Like Structured Graphene and Its High Efficiency as a Counter-Electrode Catalyst for Dye-Sensitized Solar Cells. *Angew. Chem. -In. Ed.* **52**, 9210–9214 (2013).

20. Wang, H. & Hu, Y. H. Graphene as a counter electrode material for dye-sensitized solar cells. *Energy & Environ. Sci.* **5**, 8182–8188 (2012).
21. Du, Y.-F. *et al.* One-Step Synthesis of Stoichiometric $Cu_2ZnSnSe_4$ as Counter Electrode for Dye-Sensitized Solar Cells. *Acs Appl. Mater. & Interfaces* **4**, 1796–1802 (2012).
22. Xin, X., He, M., Han, W., Jung, J. & Lin, Z. Low-Cost Copper Zinc Tin Sulfide Counter Electrodes for High-Efficiency Dye-Sensitized Solar Cells. *Angew. Chem. -In. Ed.* **50**, 11739–11742 (2011).
23. Li, G. R., Song, J., Pan, G. L. & Gao, X. P. Highly Pt-like electrocatalytic activity of transition metal nitrides for dye-sensitized solar cells. *Energy & Environ. Sci.* **4**, 1680–1683 (2011).
24. Xiao, Y. *et al.* A high performance Pt-free counter electrode of nickel sulfide/multi-wall carbon nanotube/titanium used in dye-sensitized solar cells. *J. Mater. Chem. A* **1**, 13885–13889 (2013).
25. Wang, H., Wei, W. & Hu, Y. H. Efficient ZnO-based counter electrodes for dye-sensitized solar cells. *J. Mater. Chem. A* **1**, 6622–6628 (2013).
26. Wei, W., Wang, H. & Hu, Y. H. Unusual particle-size-induced promoter-to-poison transition of ZrN in counter electrodes for dye-sensitized solar cells. *J. Mater. Chem. A* **1**, 14350–14357 (2013).
27. Xiao, Y., Wu, J., Lin, J.-Y., Tai, S.-Y. & Yue, G. Pulse electrodeposition of CoS on MWCNT/Ti as a high performance counter electrode for a Pt-free dye-sensitized solar cell. *J. Mater. Chem. A* **1**, 1289–1295 (2013).
28. Xia, J., Chen, L. & Yanagida, S. Application of polypyrrole as a counter electrode for a dye-sensitized solar cell. *J. Mater. Chem.* **21**, 4644–4649 (2011).
29. Yoo, B. *et al.* Titanium nitride thin film as a novel charge collector in TCO-less dye-sensitized solar cell. *J. Mater. Chem.* **21**, 3077–3084 (2011).
30. Zhang, T.-L., Chen, H.-Y., Su, C.-Y. & Kuang, D.-B. A novel TCO- and Pt-free counter electrode for high efficiency dye-sensitized solar cells. *J. Mater. Chem. A* **1**, 1724–1730 (2013).
31. Li, D., Huang, J. & Kaner, R. B. Polyaniline Nanofibers: A Unique Polymer Nanostructure for Versatile Applications. *Acc. Chem. Res.* **42**, 135–145 (2008).
32. Kibsgaard, J., Chen, Z., Reinecke, B. N. & Jaramillo, T. F. Engineering the surface structure of MoS2 to preferentially expose active edge sites for electrocatalysis. *Nat. Mater.* **11**, 963–969 (2012).
33. Jaramillo, T. F. *et al.* Identification of Active Edge Sites for Electrochemical H_2 Evolution from MoS_2 Nanocatalysts. *Science* **317**, 100–102 (2007).
34. Tonndorf, P. *et al.* Photoluminescence emission and Raman response of monolayer MoS_2, $MoSe_2$, and WSe_2. *Opt. Express* **21**, 4908–4916 (2013).
35. Kong, D. S. *et al.* Synthesis of MoS_2 and $MoSe_2$ Films with Vertically Aligned Layers. *Nano Lett.* **13**, 1341–1347 (2013).
36. Wang, H. *et al.* $MoSe_2$ and WSe_2 Nanofilms with Vertically Aligned Molecular Layers on Curved and Rough Surfaces. *Nano Lett.* **13**, 3426–3433 (2013).
37. Wang, Y.-C. *et al.* FeS_2 Nanocrystal Ink as a Catalytic Electrode for Dye-Sensitized Solar Cells. *Angew. Chem. -In. Ed.* **52**, 6694–6698 (2013).
38. Roy-Mayhew, J. D., Bozym, D. J., Punckt, C. & Aksay, I. A. Functionalized Graphene as a Catalytic Counter Electrode in Dye-Sensitized Solar Cells. *Acs Nano* **4**, 6203–6211 (2010).
39. Wu, M. *et al.* Economical Pt-Free Catalysts for Counter Electrodes of Dye-Sensitized Solar Cells. *J. Am. Chem. Soc.* **134**, 3419–3428 (2012).
40. Sun, H. *et al.* In Situ Preparation of a Flexible Polyaniline/Carbon Composite Counter Electrode and Its Application in Dye-Sensitized Solar Cells. *J. Phys. Chem. C* **114**, 11673–11679 (2010).
41. Kavan, L., Yum, J.-H. & Grätzel, M. Graphene Nanoplatelets Outperforming Platinum as the Electrocatalyst in Co-Bipyridine-Mediated Dye-Sensitized Solar Cells. *Nano Lett.* **11**, 5501–5506 (2011).
42. Hauch, A. & Georg, A. Diffusion in the electrolyte and charge-transfer reaction at the platinum electrode in dye-sensitized solar cells. *Electrochimica Acta* **46**, 3457–3466 (2001).
43. Wang, M. *et al.* CoS Supersedes Pt as Efficient Electrocatalyst for Triiodide Reduction in Dye-Sensitized Solar Cells. *J. Am. Chem. Soc.* **131**, 15976–15977 (2009).
44. Adachi, M., Sakamoto, M., Jiu, J. T., Ogata, Y. & Isoda, S. Determination of parameters of electron transport in dye-sensitized solar cells using electrochemical impedance spectroscopy. *J. Phys. Chem. B* **110**, 13872–13880 (2006).
45. Wang, Q., Moser, J. E. & Gratzel, M. Electrochemical impedance spectroscopic analysis of dye-sensitized solar cells. *J. Phys. Chem. B* **109**, 14945–14953 (2005).
46. Benavente, E., Santa Ana, M. A., Mendizábal, F. & González, G. Intercalation chemistry of molybdenum disulfide. *Coord. Chem. Rev.* **224**, 87–109 (2002).
47. Chen, T., Hu, W., Song, J., Guai, G. H. & Li, C. M. Interface Functionalization of Photoelectrodes with Graphene for High Performance Dye-Sensitized Solar Cells. *Adv. Funct. Mater.* **22**, 5245–5250 (2012).
48. Hua, Y. *et al.* Significant Improvement of Dye-Sensitized Solar Cell Performance Using Simple Phenothiazine-Based Dyes. *Chem. Mater.*, 2146–2153 (2013).
49. Chang, S., Li, Q., Xiao, X., Wong, K. Y. & Chen, T. Enhancement of low energy sunlight harvesting in dye-sensitized solar cells using plasmonic gold nanorods. *Energy & Environ. Sci.*, 9444–9448 (2012).

Acknowledgments

This work is supported by the CUHK Group Research Scheme, CUHK Focused Scheme B Grant "Center for Solar Energy Research" and the University Research Grant (4053012). The authors also acknowledge Bokai Zhang for taking the digital photo of the large-area electrode and Man Hau Yeung for taking the HRTEM images.

Author contributions

T.C. conceived the project and guided the research. T.C. and T.L.L. co-designed the experiments. T.L.L. fabricated the DSSC devices and conducted the electrochemical measurement. J.H. helped with electrochemical and photovoltaic characterizations. J.H. and Y.P.M. fabricated the Mo-coated soda-lime glass. T.C. and T.L.L. prepared the manuscript. All of the authors, T.L.L., J.H., B.H.W., Y.P.M., K.Y.W., Q.L., X.D.X. and T.C., discussed the results and commented on the manuscript.

Additional information

Supplementary information accompanies this paper at http://www.nature.com/scientificreports

Competing financial interests: The authors declare no competing financial interests.

How to cite this article: Lee, L.T.L. *et al.* Few-Layer $MoSe_2$ Possessing High Catalytic Activity towards Iodide/Tri-iodide Redox Shuttles. *Sci. Rep.* **4**, 4063; DOI:10.1038/srep04063 (2014).